

## Article

# Synergistic Roles of Nb and Mo in the Formation of Oxides on Fe-20Cr-25Ni-Nb Stainless Steels in High-Temperature CO<sub>2</sub>

Minrui Ran <sup>1</sup>, Qihan Wang <sup>1</sup>, Yinsheng He <sup>1</sup>, Hongyu Zhou <sup>1</sup> , Yunhao Huang <sup>2</sup>, Wenyue Zheng <sup>1,\*</sup> and Rui Tang <sup>2,\*</sup>

<sup>1</sup> National Centre for Materials Service Safety, University of Science and Technology Beijing, 30 Xueyuan Road, Haidian District, Beijing 100083, China

<sup>2</sup> Science and Technology on Reactor Fuel and Materials Laboratory, Nuclear Power Institute of China, No. 328 Huayang Changshun Avenue Section 1, Shuangliu District, Chengdu 610005, China

\* Correspondence: zheng\_wenyue@ustb.edu.cn (W.Z.); xajtrr@163.com (R.T.)

**Abstract:** Fe-20Cr-25Ni-Nb steel is an important material for developing highly compact and efficient nuclear power systems by using the supercritical CO<sub>2</sub> Brayton cycle. The in-core materials should possess excellent oxidation resistance in a high-temperature CO<sub>2</sub> environment. In this work, a new 20Cr-25Ni-Nb steel with a minor Mo addition was developed, and its oxidation behavior was investigated in a pure CO<sub>2</sub> environment at 650 °C under 3.5 MPa. The experimental results show that the oxidation kinetics of the steels followed the parabolic law with the test time, and the oxidation process was controlled by diffusion. The 20Cr-25Ni-Nb steel showed better oxidation resistance after Mo addition, which was attributed to the synergistic effects of Nb and Mo during the oxide scale formation process. In a high-temperature environment, the volatilization of Mo promoted the outward diffusion of Nb, resulting in the formation of an Nb-rich layer at the oxide/metal interface, which slowed the outward diffusion of Fe for the formation of the outermost Fe-oxide layer. Although the volatile nature of Mo at high temperatures promoted the outward diffusion of Nb, the addition of Mo had no significant influence on the overall structure of the oxide scales, which consisted of an outer Cr-rich oxide layer and an inner spinel oxide layer.



**Citation:** Ran, M.; Wang, Q.; He, Y.; Zhou, H.; Huang, Y.; Zheng, W.; Tang, R. Synergistic Roles of Nb and Mo in the Formation of Oxides on Fe-20Cr-25Ni-Nb Stainless Steels in High-Temperature CO<sub>2</sub>. *Metals* **2023**, *13*, 665. <https://doi.org/10.3390/met13040665>

Academic Editor: Rastko Vasilic

Received: 4 March 2023

Revised: 20 March 2023

Accepted: 26 March 2023

Published: 27 March 2023



**Copyright:** © 2023 by the authors. Licensee MDPI, Basel, Switzerland. This article is an open access article distributed under the terms and conditions of the Creative Commons Attribution (CC BY) license (<https://creativecommons.org/licenses/by/4.0/>).

## 1. Introduction

The Bryton cycle with supercritical carbon dioxide as the working fluid is an attractive option for energy conversion systems in next-generation nuclear reactors. It has the advantages of a higher thermal efficiency, smaller system footprint, and simpler cycle layout than that of light-water reactors [1]. In a nuclear system with a supercritical CO<sub>2</sub> Brayton cycle, particular attention needs to be paid to the oxidation of the cladding materials in the high-temperature and high-pressure CO<sub>2</sub> environment, which directly determines the heat performance and reactor thermal efficiency [2,3].

Fuel cladding for advanced gas-cooled reactors (AGRs) is manufactured from Nb-stabilized 20Cr-25Ni stainless steel (SS). The steels have excellent oxidation resistance in CO<sub>2</sub> and favorable metallurgical stability at elevated temperatures [4]. The oxidation behavior of 20Cr-25Ni-Nb alloys in high-temperature environments was previously studied [5,6]. However, the influence of Nb on the formation process of oxide scales in high-temperature CO<sub>2</sub> environments has not been systematically explained. Moreover, the contribution of Nb to oxidation resistance is not always consistent in the available literature. For example, Xu et al. [7] proposed that Nb has a positive impact on oxidation in both the kinetics and the oxide scale structures. Chen et al. [8] also suggested that Nb that is stabilized as NbC carbide precipitated at the grain boundaries can suppress the outward diffusion of the elements used to form the duplex oxide layer, which is beneficial for improving the oxidation performance of austenitic steels. Conversely, Shen et al. [9] claimed that Nb had

a negative effect on the oxidation resistance of austenitic steels because it prevented the formation of a protective Cr-rich oxide layer. Zhang et al. [10] reported that Nb could deteriorate the oxidation resistance of austenitic SS because the Nb pentoxide that formed at the oxide/matrix interface induced a large growth stress, thus increasing the risk of oxide spallation. These contradictory conclusions about the role of Nb in the oxidation behaviors of austenitic SS call for further investigation of this subject.

Mo, as a solid strength element, is always added to improve the creep and tensile strength properties at high temperatures [11,12]. However, its effect on oxidation behavior has not been widely reported. In the limited literature, it has been suggested that the combined effect of Nb and Mo has a potential influence on the oxidation behavior of austenitic SS. For example, Chen et al. indicated that intragranular  $\text{Fe}_2(\text{Nb}, \text{Mo})$  Laves precipitates and  $(\text{Nb}, \text{Mo})\text{C}$  carbides would affect the formation processes of oxide scales and, thus, change the oxidation behavior of steels [13]. Buscaill et al. reported that the presence of Mo in Nb-containing alloys promotes a pegging effect of the chromia scales, resulting in good scale adherence at high temperatures [14]. Chen found that Nb and Mo from the inner matrix could outwardly diffuse into the oxide/matrix interface or the sub-layer matrix to form  $(\text{Nb}, \text{Mo})$ -rich compounds when austenitic steels were oxidized in a high-temperature  $\text{CO}_2$  environment [8]. Although these articles described that Mo would accelerate the outward diffusion of Nb and improve the oxidation resistance of steels, the contribution of Mo to the oxidation resistance and the synergistic effects of Nb and Mo on the oxidation behavior of austenitic stainless steels have not been systematically investigated.

In this work, a new 20Cr-25Ni-Nb steel was fabricated with a minor addition of Mo (2.0 wt.%). The oxidation behavior of 20Cr-25Ni-Nb steel with and without Mo addition was studied in a high-temperature  $\text{CO}_2$  environment. The interacting roles of the key alloying elements, including Nb and Mo, in the contributions of scales after oxidation were also investigated. Finally, the synergistic effects of Nb and Mo on the formation processes of the oxide scales are discussed.

## 2. Materials and Methods

### 2.1. Materials

Two batches of 20Cr-25Ni-Nb austenitic stainless steels, namely, S1 and S2, were produced by means of vacuum induction melting and vacuum consumption melting by HBIS Group Co., Ltd. The chemical compositions of these steels used in this work were listed in Table 1. S1 represents 20Cr-25Ni-Nb with a Mo content of 2.0 wt.%, and the S2 alloy contained a higher Nb content (0.71 wt.%) without Mo addition. Both S1 and S2 had the same ratio of Nb to C,  $[\text{Nb}/\text{C} + \text{N}] = 7.7$ , to prevent the precipitation of a second phase other than fine NbC particles [5]. The processing of the materials and the production process for the alloys was similar to that used for AGR claddings reported in other studies [15]. In this work, the as-received 20Cr-25Ni-Nb ingots were forged and hot rolled at  $1200^\circ\text{C}$ , followed by cold rolling after removing the surface layer. The deformation ratio of forging and hot rolling was 50%, and the cold rolling was carried out with a reduction in thickness of ~25%. Then, the materials were subjected to a stable heat treatment at  $930^\circ\text{C}$  for one hour in an inert atmosphere to precipitate a fine dispersion of NbC in the matrix.

**Table 1.** Chemical compositions of the materials used in this work (wt.%).

Materials	Fe	Cr	Ni	Nb	N	C	Si	Mn	Mo
S1	Bal.	20.0	24.8	0.51	0.015	0.05	0.6	0.6	2.0
S2	Bal.	20.2	24.8	0.71	0.065	0.04	0.6	0.7	-

### 2.2. Oxidation Tests

The two materials were machined via electro-discharge into specimens with a dimension of  $20 \times 10 \times 2 \text{ mm}^3$ . This was followed by mechanical grinding with 600 grit

silicon carbide paper; then, the specimens were ultrasonically cleaned in ethanol. Triplicate specimens of each material were subjected to an oxidation test, which was carried out in a horizontal furnace equipped with an enclosed Ni-based alloy heater tube with an outer diameter and wall thickness of 60 mm and 4.5 mm, respectively. The constant-temperature zone of the tube was 200 mm long, and the temperature variation was within  $\pm 1$  °C. Static isothermal oxidation tests were performed in a high-purity CO<sub>2</sub> (99.99%) environment at 650 °C and 3.5 MPa for a time period of up to 1000 h. Before the tests, the tube was thoroughly purged with CO<sub>2</sub>. The weights of two samples of each material prior to and after 200 h, 500 h, and 1000 h of exposure were measured by using an electronic microbalance (Greifensee, Switzerland, Mettler Toledo XPR 225) with a readability of 10<sup>-5</sup> g. The mean value of weight gain was taken as an indicator of oxidation resistance.

### 2.3. Characterization Procedures

Before oxidation, samples S1 and S2 were metallographically polished and etched with a solution of 10 vol.% oxalic acid. The original microstructures of samples S1 and S2 were observed by using an optical microscope (OM, Tokyo, Japan, Olympus, GX51) and a scanning electron microscope (SEM, Jena, Germany, Zeiss, SUPRA55) equipped with an energy-dispersive spectrometer (EDS).

After oxidation, the surface morphology of the oxidized samples was investigated through SEM-EDS. The surface oxides were then characterized with a laser confocal Raman spectrometer (Braunschweig, Germany, WItech, Alpha 300RA) and through X-ray photoelectron spectroscopy (XPS, Kyoto, Japan, Shimadzu, ultra-DLD). Cross-sectional samples were observed with the SEM-EDS and an electron probe X-ray microanalyzer (EPMA, Tokyo, Japan, Japan Electronics Corporation, JXA-8530F Plus).

## 3. Results

### 3.1. Microstructure of 20Cr-25Ni-Nb SS

Figure 1 presents OM images of samples S1 and S2, which showed similarities in their microstructures, i.e., grain size (Figure 1a,b) and a uniform distribution of NbC (insert in Figure 1c,d) within the grains and at grain boundaries. The results suggested that Mo did not have a significant effect on the microstructure in the steels produced for this study. It helped to exclude the effects of grain size or grain boundary density on the oxidation behaviors of the two steel samples.

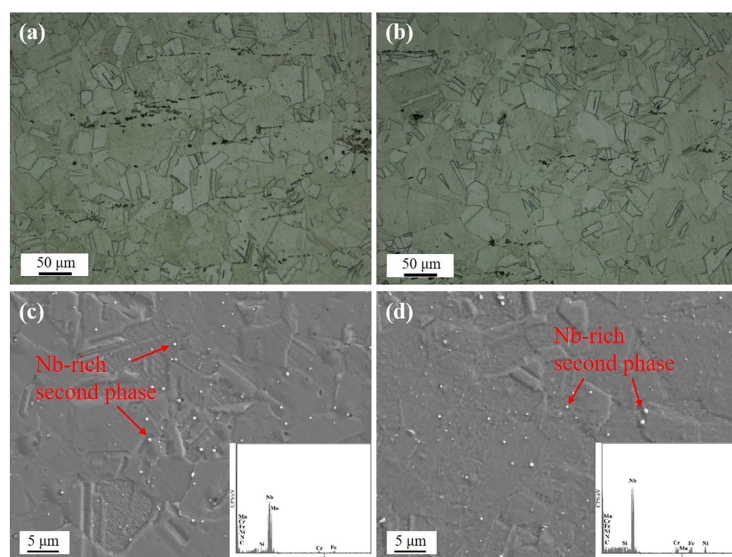


**Figure 1.** Microstructures of the 20Cr-25Ni-Nb samples: (a,b) OM and (c,d) SEM images of samples S1 and S2, respectively.

### 3.2. Oxidation Kinetics

Figure 2 shows the average weight gains of the two samples as a function of exposure time in high-temperature CO<sub>2</sub>. The weight gain of both samples followed an approximately parabolic trend as a function of exposure time, indicating that the oxidation kinetics were a diffusion-controlled process. In all test samples, the weight gains of the S1 samples were consistently lower than those of the S2 samples, confirming the enhancement of oxidation resistance with the addition of Mo. The variation in the change in mass with time can be fitted as follows [16]:

$$\frac{\Delta m}{A} = k \times t^n$$

where  $\Delta m/A$  (in mg/dm<sup>2</sup>) is the weight gain per unit area during time  $t$  (h),  $k$  (in mg dm<sup>-2</sup> h<sup>-n</sup>) is the oxidation constant, and  $n$  is the reaction order. Despite the slight differences in the  $k$  values of the two samples, the  $n$  value of sample S1 was  $\sim 0.31$ , which was relatively lower than that of the S2 specimen, which was  $\sim 0.39$ . The smaller  $n$  values for sample S1 indicated that its weight change was less affected by the exposure time. With the fitted values and the weight gain results, it was confirmed that the oxidation resistance of sample S1 was better than that of sample S2.

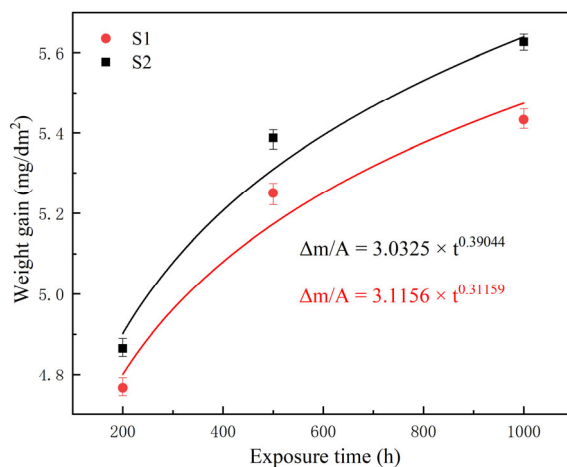
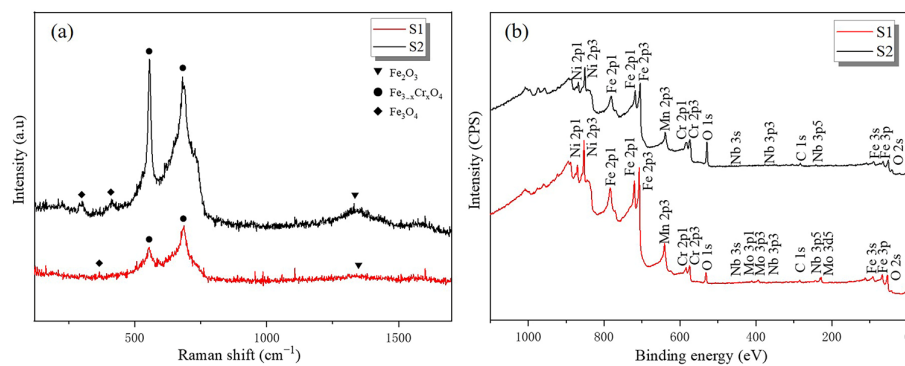


**Figure 2.** Oxidation kinetic curves of samples S1 and S2 in CO<sub>2</sub> at 650 °C under 3.5 MPa for 1000 h.

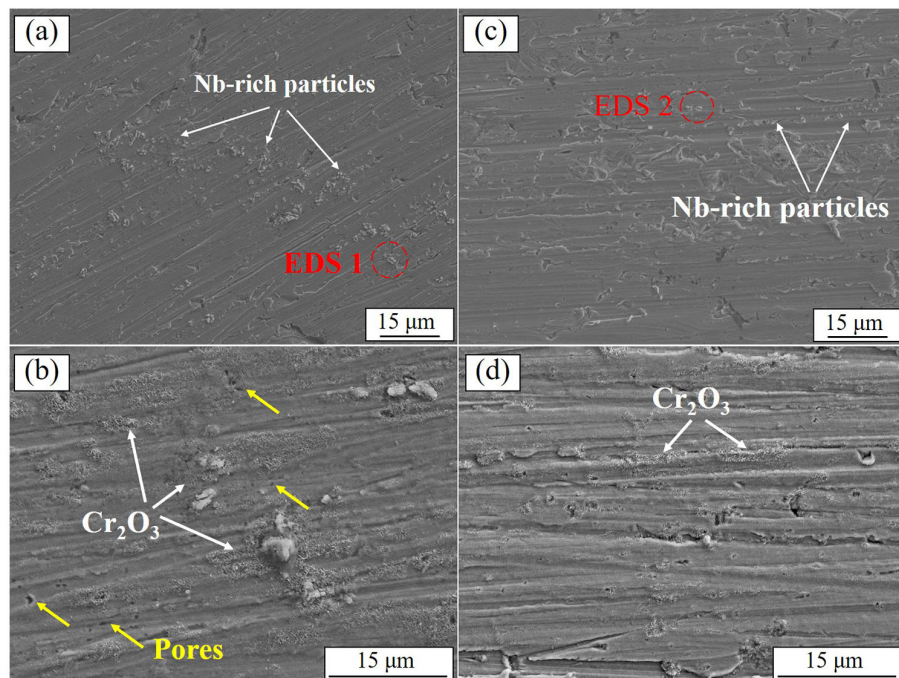
### 3.3. Surface Oxide Features

Figure 3a presents the Raman spectra of the two investigated samples after exposure to high-temperature CO<sub>2</sub> at 650 °C under 3.5 MPa for 1000 h. The results indicate that the surface oxide scales grown on all tested samples were composed primarily of magnetite (Fe<sub>3</sub>O<sub>4</sub>), spinel-type Fe<sub>3-x</sub>Cr<sub>x</sub>O<sub>4</sub> ( $0 < x < 2$ ), and a small amount of hematite (Fe<sub>2</sub>O<sub>3</sub>), which agreed with the data reported in the literature [17]. Figure 3b shows the results of the XPS analysis of the oxidized surfaces of samples S1 and S2 after 1000 h of exposure. It was easy to find the signals of Cr and Fe, which suggested the presence of corresponding oxides in the outermost oxide layer. A small peak of Mo signals in the XPS spectrum of sample S1 could be seen, indicating the existence of Mo-containing oxides on the surface.

Figure 4 shows the surface SEM images of samples S1 and S2 after being oxidized in a CO<sub>2</sub> environment. Even after exposure for 1000 h, the abrasion lines generated by mechanical grinding prior to the oxidation tests were still visible on the surfaces of samples S1 and S2, as shown in Figure 4b,d, suggesting the excellent oxidation resistance of the developed steels when compared to that of 310S with a higher Cr content under similar conditions [18]. After 500 h of exposure (Figure 4a,c), many small cluster-like Nb-rich particles emerged on the surfaces of both S1 and S2; these were confirmed to be the original NbC, as shown by the corresponding EDS analysis (Table 2), which agreed with previously reported data [19].



**Figure 3.** Raman spectra (a) and XPS results (b) of the investigated samples tested in  $\text{CO}_2$  at  $650^\circ\text{C}$  under 3.5 MPa for 1000 h.



**Figure 4.** Surface SEM images of samples S1 (a,b) and S2 (c,d) oxidized in  $\text{CO}_2$  at  $650^\circ\text{C}$  under 3.5 MPa for 500 h (a,c) and 1000 h (b,d), respectively.

**Table 2.** EDS results (wt.%) of the micro-zones marked in Figure 4.

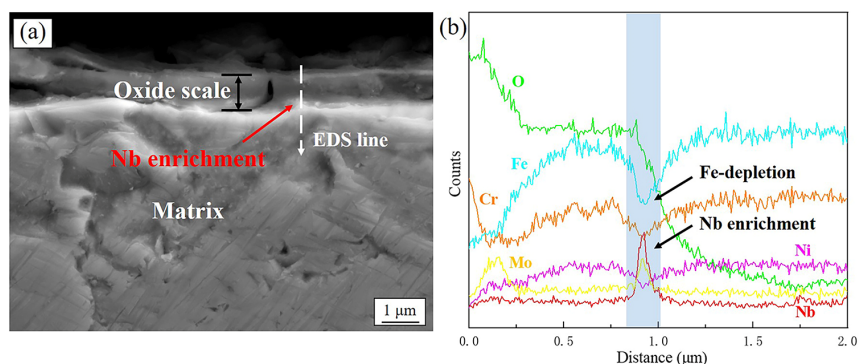
Point	C	O	Si	Fe	Cr	Ni	Nb	Mo
EDS 1	8.32	33.26	0.32	9.76	7.41	1.29	35.50	4.14
EDS 2	7.58	28.45	0.54	16.98	6.69	3.75	35.97	0.04

When the exposure time was extended to 1000 h, the number of NbC particles on the surfaces of S1 and S2 slightly decreased as they became embedded under the growing oxide scales, as shown in Figure 4b,d. Additionally, some needle-like oxides were observed to be formed around these Nb-rich particles, as indicated by the white arrows in Figure 4b,d; these were suggested to be Cr-rich oxides [20]. Some tiny pores appeared on the surface of S1, as shown in Figure 4b (marked by yellow arrows), which may have been related to the evaporation of  $\text{MoO}_3$  [21].

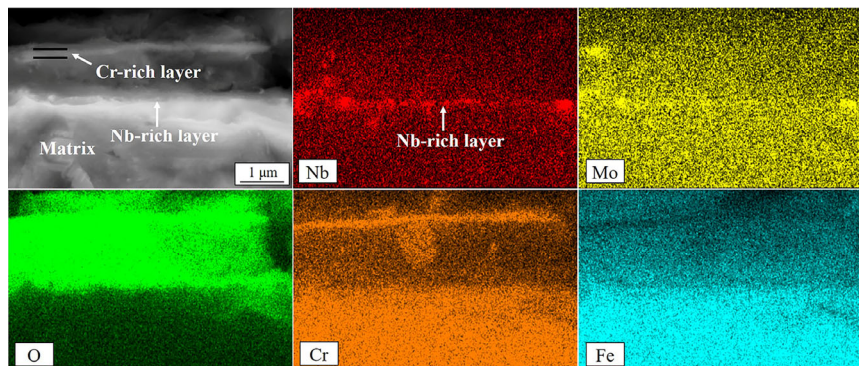
### 3.4. Cross-Sectional Observation of the Oxide/Matrix Interface

Figure 5 presents the cross-sectional SEM and corresponding EDS results of sample S1 after exposure for 1000 h. The total thickness of the oxide scales was less than one

micrometer, as shown in Figure 5a. The EDS line profile results (Figure 5b) showed that the outer oxide layer was enriched with Cr, with a Nb-rich layer at the oxide/matrix interface. A further investigation with a greater magnification showed that the scales were composed of an outer dense Cr-rich layer and an underlying thick spinel oxide layer, as shown in Figure 6. Enrichment with Fe was not found on the outermost surface, indicating that the outward diffusion of Fe was insufficient. At the oxide/matrix interface, there was a continuous Nb- and Mo-enriched layer, suggesting that the original stabilized Nb and Mo in the matrix had diffused outward to the oxide/substrate interface after high-temperature oxidation.



**Figure 5.** Cross-sectional SEM (a) with the corresponding EDS line profile (b) images of sample S1 after exposure to  $\text{CO}_2$  at  $650\text{ }^\circ\text{C}$  under 3.5 MPa for 1000 h.



**Figure 6.** Cross-sectional SEM with corresponding EDS mapping images of sample S1 after exposure to  $\text{CO}_2$  at  $650\text{ }^\circ\text{C}$  under 3.5 MPa for 1000 h.

Figure 7 shows the cross-sectional SEM image and corresponding EDS results of sample S2 after exposure for 1000 h. Compared with sample S1, there were no significant differences in the thickness and structure of the oxide scales formed on sample S2, as shown in Figure 7a. Enrichment with Nb also mainly appeared at the oxide/matrix interface according to the EDS line profile, as shown in Figure 7b. The high-magnification SEM image (Figure 8) shows that the oxide scales consisted of an outer Cr-rich layer and an inner spinel oxide, as confirmed by the corresponding EDS mapping results. Further observation (Figure 8) revealed that there was also enrichment with Nb at the oxide/matrix interface, but no continuous Nb-rich layer were formed as they were in sample S1, indicating the lower outward diffusion of Nb in sample S2.

To further confirm the distribution of elements in the oxide scales, the cross-sectional areas of samples S1 and S2 with 1000 h of exposure were investigated through EPMA, as shown in Figure 9. A distinct Cr-rich layer with only a small amount of Fe above it could be easily observed in samples S1 and S2, suggesting that the initially formed Cr-rich layer on the surface still maintained good structural integrity and could effectively slow the outward diffusion of metallic elements. For sample S1, Nb was accumulated beneath the

oxide scales, forming a continuous Nb-rich layer at the oxide/matrix interface (Figure 9a). Figure 9b shows that the distribution of Nb in sample S2 was relatively uniform, and no obvious enrichment near the oxide scales was observed, although sample S2 had a higher Nb content than that of S1. The reason for this phenomenon may be that the addition of Mo led to more enrichment with Nb, and the promoting effect of Mo on the diffusion of Nb will be further discussed in the next section.

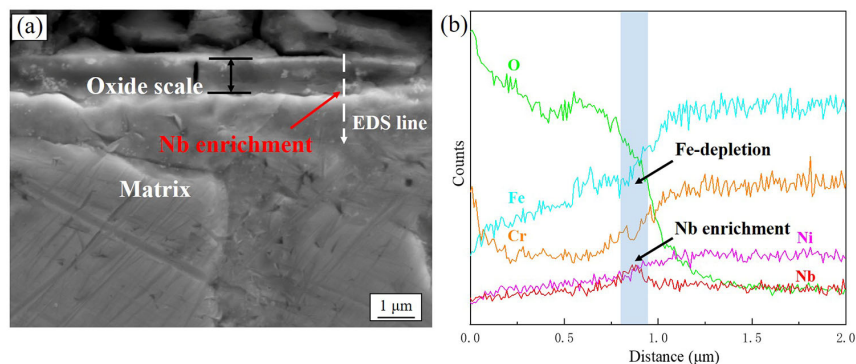


**Figure 7.** Cross-sectional SEM (a) with the corresponding EDS line profile (b) images of sample S2 after exposure to  $\text{CO}_2$  at  $650^\circ\text{C}$  under 3.5 MPa for 1000 h.

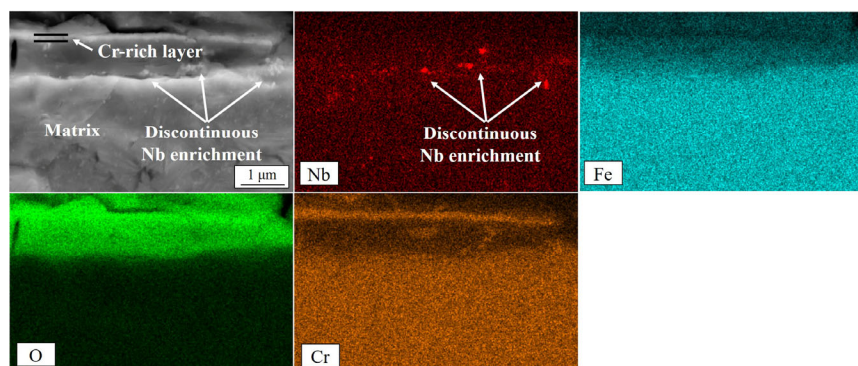


**Figure 8.** Cross-sectional SEM with the corresponding EDS mapping images of sample S2 after exposure to  $\text{CO}_2$  at  $650^\circ\text{C}$  under 3.5 MPa for 1000 h.

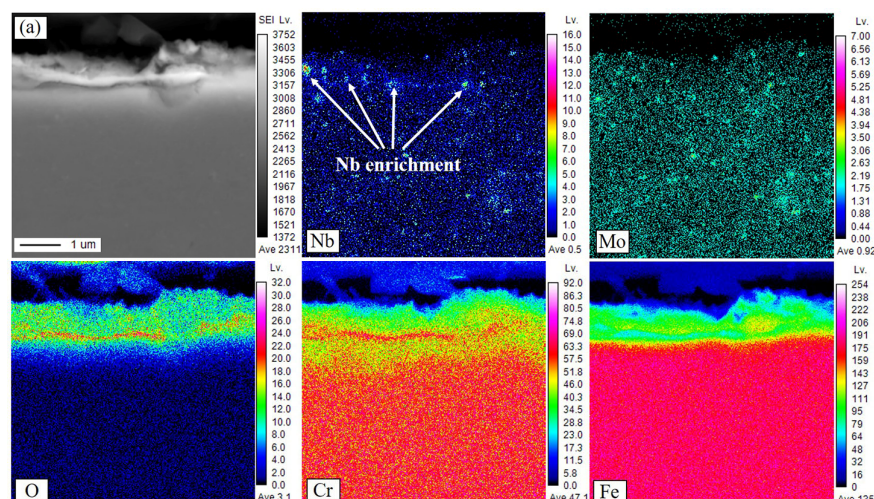


**Figure 9. Cont.**

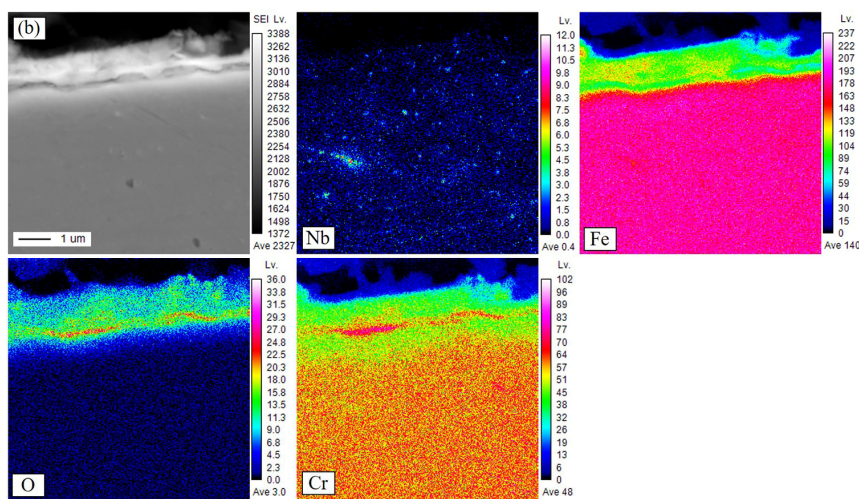


**Figure 9.** Cross-sectional morphologies and corresponding EPMA results of (a) S1 and (b) S2 after exposure to  $\text{CO}_2$  at  $650\text{ }^\circ\text{C}$  under  $3.5\text{ MPa}$  for  $1000\text{ h}$ .

#### 4. Discussion

##### 4.1. Oxide Scale Formation

Figure 10 presents a schematic diagram of the formation process of the oxide scales on 20Cr-25Ni-Nb steels with and without the addition of Mo. In the initial stage of oxidation (Figure 10a), the formation and growth of  $\text{Cr}_2\text{O}_3$  were predominant because of the higher oxygen affinity of Cr and its relatively rapid diffusion within the substrate, although all of the major elements (Fe, Cr, Mn, Ni) in the steel had equal opportunity to form oxides by reacting with  $\text{CO}_2$  [22,23]. The formation process of chromia can be described by Equation (1) [24]:

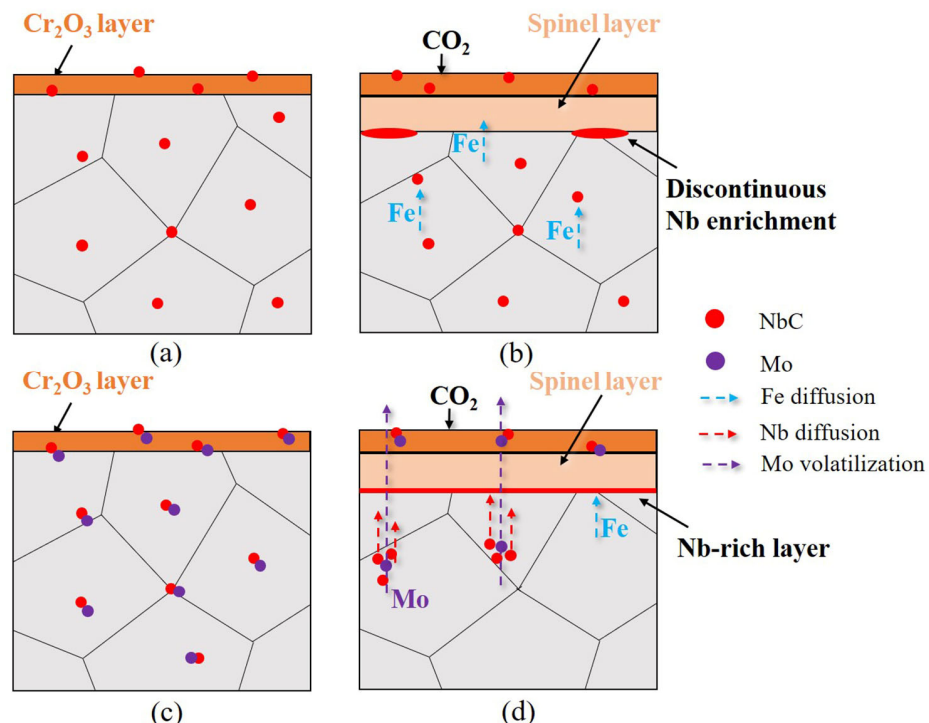


**Figure 10.** Schematic diagram of the formation process of oxide scales: (a,b) S2 and (c,d) S1.

As the oxidation time increased,  $\text{CO}_2$  molecules were gradually transported inward through defect tunnels (such as grain boundaries and pores) in the  $\text{Cr}_2\text{O}_3$  layer and then reacted with the metallic elements at the matrix/oxide interface to form spinel oxides [25]. These oxides constituted most of the oxide layer, which was located between the chromia layer and the matrix in S1, as shown in Figure 10b. The formation process of chromia can be expressed as follows [26,27]:



Alloyed Nb existed in the 20Cr-25Ni-Nb in the form of NbC, which already existed on the surface before oxidation, as shown in Figure 10a. NbC particles are relatively thermodynamic stable, and most of them cannot be oxidized to form niobium oxides [19]. The ultimate fate of the NbC that was present on the surface was to be gradually covered by the growing oxide scales, as shown in Figure 10b.

#### 4.2. Synergistic Effect of Nb and Mo on Scale Formation

Nb played a significant role in the oxidation processes of 20Cr-25Ni-Nb stainless steel by following two routes: On the one hand, substantial and uniformly distributed NbC precipitates in the alloy matrix could prevent the outward diffusion of metallic elements (particularly Fe) during the formation process of the oxide scales, as shown in Figure 10b. This effect could be seen from the cross-sectional EDS line scanning results for S1 (Figure 5b), where Nb enrichment and Fe depletion concurrently occurred at a depth of ~0.8  $\mu\text{m}$ . Below the chromia layer, from the surface to the matrix direction, the Fe content should continuously increase and eventually stabilize. However, there was an obvious Fe depletion layer of tens of nanometers in the region at a depth of ~0.8  $\mu\text{m}$ , where Nb was enriched. Similarly, but less obviously, Nb enrichment and Fe depletion were also seen in sample S2, as shown in Figure 7b. The research by Xu et al. also suggested that NbC that precipitated at GBs effectively hindered the outward diffusion of Fe and Ni, thereby improving the oxidation performance of austenitic alloys [7].

On the other hand, the slightly soluble Nb dissociated from NbC near oxide scales could increase the Cr activity and further enhance the volume diffusion of Cr to the surface, thus supporting chromia formation. This supposition can be supported by the top-view SEM images of the oxidized samples (Figure 4), which showed some needle-like oxides to be present around the Nb-rich particles on the surface of samples S1 and S2. A similar observation was reported in the previous literature, where Nb promoted the formation of  $\text{Cr}_2\text{O}_3$  on the surface of 22Cr-25Ni steel in high-temperature air [28].

The addition of Mo to stainless steels is usually used to improve their high-temperature mechanical properties [11], their resistance to pitting oxidation [29], and their stress corrosion cracking [30]. Abramov et al. proposed that the use of Mo could improve the corrosion resistance of low-carbon austenitic steels at high temperatures [31]. In this work, the beneficial effect of Mo on oxidation performance was also shown, which was likely due to the formation of a continuous Nb-rich layer at the oxide/matrix interface.

After the addition of Mo to the alloy, NbC combined with it to form (Nb, Mo)-rich compounds in the alloy matrix [32]. The beneficial effect of Mo on the outward diffusion of Nb was also reported in a previous study, but the exact mechanism involved was not clear [8,13]. It is well known that the presence of Mo is redistributed during oxidation due to the formation of diffusively mobile oxides with a low melting point [33]. At high temperatures, the volatilization of Mo directly ‘carries’ Nb from the matrix to the oxide/matrix interface if Nb and Mo have strong binding forces. Alternatively, vacancies could form around Nb atoms after Mo has dissociated from (Nb, Mo)-rich particles and volatilized to the outer surface; such vacancies can provide the driving force for the outward diffusion of Nb toward the oxide/matrix interface. The results of cross-sectional EDS mapping (Figures 6 and 8) and EPMA (Figure 9) present evidence for the above speculations. A continuous Nb-rich layer appeared at the oxide/matrix interface in sample S1 with a Mo content of 2.00 wt.%, as shown by the arrows in Figures 6 and 9a. One can

predict that without the ‘carrying outward’ action of Mo, a Nb-rich layer would not form at the oxide/matrix interface, and this was indeed the case in sample S2 (Figure 7). Despite the different mechanisms at work, in austenitic stainless steels containing Nb, the addition of Mo increased the Nb concentration at the oxide/matrix interface, which slowed the outward diffusion of the metallic elements, especially Fe. In addition, the addition of Mo to Nb-containing steels mildly promoted the precipitation of NbC, resulting in a higher density and smaller average size of Nb-rich carbide precipitates [34]. This phenomenon can mainly be attributed to the decrease in interfacial energy between the precipitate and the matrix, which lowered the energy barrier of nucleation of precipitation in the early stage and the coarsening kinetics of precipitation in the later stage [35]. The dispersed distribution of fine Nb-rich carbides makes it difficult for metallic elements, especially Fe, to diffuse outward, thus suppressing the formation of the outermost Fe oxide layer [36].

The above results indicate that Mo addition is beneficial for improving the oxidation resistance of 20Cr-25Ni-Nb steels due to the synergistic effects of Nb and Mo in the formation of oxides. Meanwhile, because Mo is a solid-solution-strengthening element, the addition of Mo can also improve the high-temperature mechanical properties of steels. Therefore, the addition of Mo can improve the comprehensive performance of stainless steel. In fact, many pressurized water reactors (PWR) contain in-core components made of Mo-containing stainless steels, such as 316 NG, but there may be some minor limitations to consider, such as contamination of the in-core coolant environment when an alloy is used as fuel cladding due to Mo volatilization [37,38].

## 5. Conclusions

The oxidation behavior of 20Cr-25Ni-Nb stainless steels with/without Mo addition was investigated in a high-temperature CO<sub>2</sub> environment. The following conclusions can be drawn:

- (1) The oxidation kinetics of the steels followed a parabolic law, as shown in the measurements of weight gain.
- (2) The steel with 2.0 wt.% Mo showed a better oxidation resistance than that of the Mo-free sample. This was attributed to the formation of a Nb-rich layer at the oxide/matrix interface, which slowed the outward diffusion of Fe and, thus, slowed down the formation of the outermost Fe-oxide layer. The volatile nature of Mo at high temperatures promoted the outward diffusion of Nb, leading to the formation of this Nb-rich layer.
- (3) The addition of Mo at a level of 2.0 wt.% had no significant influence on the overall oxide scale structure, which consisted of an outer Cr-rich oxide layer and an inner spinel oxide layer.

**Author Contributions:** Conceptualization, M.R. and W.Z.; methodology, M.R.; software, M.R.; validation, Q.W., H.Z. and Y.H. (Yingsheng He); formal analysis, Y.H. (Yunhao Huang); investigation, Y.H. (Yunhao Huang) and R.T.; resources, R.T.; data curation, R.T.; writing—original draft preparation, M.R.; writing—review and editing, Q.W., Y.H. (Yingsheng He) and W.Z.; visualization, M.R.; supervision, M.R.; project administration, W.Z.; funding acquisition, R.T. All authors have read and agreed to the published version of the manuscript.

**Funding:** This research was funded by the National Key Research and Development Program of China (grant number 2018YFE0116200), and the Scientific Research Program for Young Talent of China National Nuclear Corporations (grant number NPIC-k301007038).

**Data Availability Statement:** Available upon request.

**Acknowledgments:** The authors would like to thank Li Gong for the insightful comments and motivating discussions on this manuscript.

**Conflicts of Interest:** The authors declare no conflict of interest.

## References

- Ahn, Y.; Bae, S.J.; Kim, M.; Cho, S.K.; Baik, S.; Lee, J.I.; Cha, J.E. Review of supercritical CO<sub>2</sub> power cycle technology and current status of research and development. *Nucl. Eng. Technol.* **2015**, *47*, 647–661. [[CrossRef](#)]
- Liang, Z.; Gui, Y.; Wang, Y.; Zhao, Q. Corrosion performance of heat-resisting steels and alloys in supercritical carbon dioxide at 650 °C and 15 MPa. *Energy* **2019**, *175*, 345–352. [[CrossRef](#)]
- Holcomb, G.R.; Carney, C.; Doğan, Ö.N. Oxidation of alloys for energy applications in supercritical CO<sub>2</sub> and H<sub>2</sub>O. *Corros. Sci.* **2016**, *109*, 22–35. [[CrossRef](#)]
- Yang, C.H.; Labun, P.A.; Welsch, G.; Mitchell, T.E.; Bennett, M.J. Influence of ion implantation on the microstructure of oxide scales formed on a 20Cr/25Ni/Nb-stabilized stainless steel in carbon dioxide at 825° C. *J. Mater. Sci.* **1987**, *22*, 449–458. [[CrossRef](#)]
- Allen, G.C.; Tempest, P.A.; Tyler, J.W.; Wild, R.K. Oxidation behavior of 20%Cr/25%Ni/Nb stabilized stainless steel in CO<sub>2</sub> environments. *Oxid. Met.* **1984**, *21*, 187–203. [[CrossRef](#)]
- Ding, R.; Taylor, M.; Evans, H.; Mowforth, C.; Smith, N.; Chiu, Y.; Connolly, B. Influence of low CO concentration on catalysed carbon deposition on 20Cr25Ni steel in CO<sub>2</sub> environments containing ethene. *Corros. Sci.* **2018**, *143*, 56–64. [[CrossRef](#)]
- Xu, Y.-X.; Lu, J.-T.; Yang, X.-W.; Yan, J.-B.; Li, W.-Y. Effect and role of alloyed Nb on the air oxidation behaviour of Ni-Cr-Fe alloys at 1000 °C. *Corros. Sci.* **2017**, *127*, 10–20. [[CrossRef](#)]
- Chen, H.; Kim, S.H.; Kim, C.; Chen, J.; Jang, C. Corrosion behaviors of four stainless steels with similar chromium content in supercritical carbon dioxide environment at 650 °C. *Corros. Sci.* **2019**, *156*, 16–31. [[CrossRef](#)]
- Shen, L.; Wu, B.; Zhao, K.; Peng, H.; Wen, Y. Reason for negative effect of Nb addition on oxidation resistance of alumina-forming austenitic stainless steel at 1323 K. *Corros. Sci.* **2021**, *191*, 109754. [[CrossRef](#)]
- Zhang, X.; Li, D.; Li, Y.; Lu, S. Oxidation behaviors of Fe-25Cr-20Ni- $\chi$ Nb austenitic weld metals at 1100 °C in ambient air: Role of elemental niobium. *Corros. Sci.* **2019**, *159*, 108137. [[CrossRef](#)]
- Zhou, Z.; Sun, S.; Zou, L.; Schneider, Y.; Schmauder, S.; Wang, M. Enhanced strength and high temperature resistance of 25Cr20Ni ODS austenitic alloy through thermo-mechanical treatment and addition of Mo. *Fusion Eng. Des.* **2019**, *138*, 175–182. [[CrossRef](#)]
- Jiang, L.; Marceau, R.; Dorin, T.; Yin, H.; Sun, X.; Hodgson, P.; Stanford, N. The Effect of Molybdenum on Precipitation Behaviour in Austenite of Strip-Cast Steels Containing Niobium. *Metals* **2020**, *10*, 1330. [[CrossRef](#)]
- Chen, H.; Kim, S.H.; Long, C.; Kim, C.; Jang, C. Oxidation behavior of high-strength FeCrAl alloys in a high-temperature supercritical carbon dioxide environment. *Prog. Nat. Sci. Mater. Int.* **2018**, *28*, 731–739. [[CrossRef](#)]
- Buscail, H.; Rolland, R.; Issartel, C.; Rabaste, F.; Riffard, F.; Aranda, L.; Vilasi, M. Effects of water vapour on the oxidation of a nickel-base 625 alloy between 900 and 1100 °C. *J. Mater. Sci.* **2011**, *46*, 5903–5915. [[CrossRef](#)]
- Al-Shater, A.; Engelberg, D.; Lyon, S.; Donohoe, C.; Walters, S.; Whillock, G.; Sherry, A. Characterization of the stress corrosion cracking behavior of thermally sensitized 20Cr-25Ni stainless steel in a simulated cooling pond environment. *J. Nucl. Sci. Technol.* **2017**, *54*, 742–751. [[CrossRef](#)]
- Li, K.; Zeng, Y.; Luo, J.-L. Corrosion of SS310 and Alloy 740 in high temperature supercritical CO<sub>2</sub> with impurities H<sub>2</sub>O and O<sub>2</sub>. *Corros. Sci.* **2021**, *184*, 109350. [[CrossRef](#)]
- Martinelli, L.; Desgranges, C.; Rouillard, F.; Ginestar, K.; Tabarant, M.; Rousseau, K. Comparative oxidation behaviour of Fe-9Cr steel in CO<sub>2</sub> and H<sub>2</sub>O at 550 °C: Detailed analysis of the inner oxide layer. *Corros. Sci.* **2015**, *100*, 253–266. [[CrossRef](#)]
- Oleksak, R.P.; Holcomb, G.R.; Carney, C.S.; Doğan, N. Carburization susceptibility of chromia-forming alloys in high-temperature CO<sub>2</sub>. *Corros. Sci.* **2022**, *206*, 110488. [[CrossRef](#)]
- Tyler, J.W. Characterization Of The Initial Oxide formed on annealed and unannealed 20Cr-25Ni-Nb-stabilized steel in 50 torr CO<sub>2</sub> at 973 K. *Oxid. Met.* **1985**, *24*, 149–176. [[CrossRef](#)]
- Firouzdor, V.; Sridharan, K.; Cao, G.; Anderson, M.; Allen, T. Corrosion of a stainless steel and nickel-based alloys in high temperature supercritical carbon dioxide environment. *Corros. Sci.* **2013**, *69*, 281–291. [[CrossRef](#)]
- Tan, L.; Anderson, M.; Taylor, D.; Allen, T. Corrosion of austenitic and ferritic-martensitic steels exposed to supercritical carbon dioxide. *Corros. Sci.* **2011**, *53*, 3273–3280. [[CrossRef](#)]
- Pour-Ali, S.; Kiani-Rashid, A.-R.; Babakhani, A.; Norouzi, M.; Virtanen, S. New insights into the effects of surface nanocrystallization on the oxidation of 321 austenitic stainless steel in a humid oxygen environment at 1000 °C. *Corros. Sci.* **2019**, *147*, 231–245. [[CrossRef](#)]
- Li, Y.; Wang, S.; Sun, P.; Xu, D.; Ren, M.; Guo, Y.; Lin, G. Early oxidation mechanism of austenitic stainless steel TP347H in supercritical water. *Corros. Sci.* **2017**, *128*, 241–252. [[CrossRef](#)]
- Lee, H.J.; Subramanian, G.O.; Kim, S.H.; Jang, C. Effect of pressure on the corrosion and carburization behavior of chromia-forming heat-resistant alloys in high-temperature carbon dioxide environments. *Corros. Sci.* **2016**, *111*, 649–658. [[CrossRef](#)]
- Young, D.J.; Nguyen, T.D.; Felfer, P.; Zhang, J.; Cairney, J.M. Penetration of protective chromia scales by carbon. *Scr. Mater.* **2014**, *77*, 29–32. [[CrossRef](#)]
- Wood, G.; Whittle, D. The mechanism of breakthrough of protective chromium oxide scales on Fe-Cr alloys. *Corros. Sci.* **1967**, *7*, 763–782. [[CrossRef](#)]
- Zhao, S.; Xie, X.; Smith, G.D. The oxidation behavior of the new nickel-based superalloy Inconel 740 with and without Na<sub>2</sub>SO<sub>4</sub> deposit. *Surf. Coat. Technol.* **2004**, *185*, 178–183. [[CrossRef](#)]
- Huang, S.-Y.; Tsai, W.-T.; Pan, Y.-T.; Kuo, J.-C.; Chen, H.-W.; Lin, D.-Y. Effect of Niobium Addition on the High-Temperature Oxidation Behavior of 22Cr25NiWCoCu Stainless Steel in Air. *Metals* **2019**, *9*, 975. [[CrossRef](#)]

29. Mesquita, T.J.; Chauveau, E.; Mantel, M.; Nogueira, R.P. A XPS study of the Mo effect on passivation behaviors for highly controlled stainless steels in neutral and alkaline conditions. *Appl. Surf. Sci.* **2013**, *270*, 90–97. [[CrossRef](#)]
30. Monnot, M.; Roche, V.; Estevez, R.; Mantel, M.; Nogueira, R.P. Molybdenum effect on the Sulfide Stress Corrosion of a super martensitic stainless steel in sour environment highlighted by Electrochemical Impedance Spectroscopy. *Electrochim. Acta* **2017**, *252*, 58–66. [[CrossRef](#)]
31. Abramov, A.V.; Polovov, I.B.; Rebrin, O.I.; Lisienko, D.G. Corrosion of austenitic steels and their components in vanadium-containing chloride melts. *Russ. Metall.* **2014**, *2014*, 624–632. [[CrossRef](#)]
32. Zhang, Z.; Wang, Z.; Li, Z.; Sun, X. Microstructure Evolution and Precipitation Behavior in Nb and Nb-Mo Microalloyed Fire-Resistant Steels. *Metals* **2023**, *13*, 112. [[CrossRef](#)]
33. Leont'ev, L.I.; Udoeva, L.Y.; Chumarev, V.M.; Gulyaeva, R.I.; Pankratov, A.A.; Sel'menskikh, N.I.; Zhidovinova, S.V. Microstructure of a complex Nb-Si-based alloy and its behavior during high-temperature oxidation. *Russ. Metall.* **2016**, *2016*, 67–75. [[CrossRef](#)]
34. Wang, Z.; Zhu, X.; Liu, W. Influence of Mo on Tempering Precipitation in Nb-Mo-V Microalloyed Steels. *Chin. J. Mater. Res.* **2010**, *24*, 217–224.
35. Pan, H.; Ding, H.; Cai, M.; Kibaroglu, D.; Ma, Y.; Song, W. Precipitation behavior and austenite stability of Nb or Nb-Mo micro-alloyed warm-rolled medium-Mn steels. *Mater. Sci. Eng. A* **2019**, *766*, 138371. [[CrossRef](#)]
36. Xu, Y.; Lu, J.; Li, W.; Yang, X. Oxidation behaviour of Nb-rich Ni-Cr-Fe alloys: Role and effect of carbides precipitates. *Corros. Sci.* **2018**, *140*, 252–259. [[CrossRef](#)]
37. Guzonas, D.; Novotny, R.; Penttilä, S.; Toivonen, A.; Zheng, W. (Eds.) *Materials and Water Chemistry for Supercritical Water-cooled Reactors*; Woodhead Publishing: Boston, UK, 2018; pp. 139–218.
38. Fujii, T.; Yamana, H.; Takamiya, K.; Watanabe, M.; Moriyama, H. Adsorption of fission products on a metal surface in nitric acid solutions: Radiochemical study using a multitracer. *J. Radioanal. Nucl. Chem.* **2002**, *253*, 199–204. [[CrossRef](#)]

**Disclaimer/Publisher's Note:** The statements, opinions and data contained in all publications are solely those of the individual author(s) and contributor(s) and not of MDPI and/or the editor(s). MDPI and/or the editor(s) disclaim responsibility for any injury to people or property resulting from any ideas, methods, instructions or products referred to in the content.